Bulletin of Electrical Engineering and Informatics
Vol. 15, No. 6, December 2026, pp. 4815~4824
ISSN: 2302-9285, DOI: 10.11591/eei.v15i6.13104

Observer-based non-singular terminal sliding mode control for robust regulation of high-gain DC–DC converters

Thanh-Lam Le, Nguyen Thi Bich Mai
Faculty of Electrical and Electronics Engineering, Ho Chi Minh City University of Technology and Engineering, Ho Chi Minh City, Vietnam

Article Info

Article history:

Received Apr 16, 2026
Revised Aug 23, 2026
Accepted Sep 12, 2026

Keywords:

Disturbance rejection
Energy conversion systems
High-performance control
Observer-based control
Renewable energy system
Robust control

ABSTRACT

High-gain capacitor-based boost converters (HG-CBCs) require robust voltage regulation despite nonlinear internal coupling, parameter variations, and limited feedback sensing. An output-feedback architecture is developed by combining a signed-power non-singular terminal sliding mode controller (NTSMC) with a linear extended state observer (LESO), which reconstructs the output-voltage derivative and lumped output-channel dynamics from the measured voltage alone. The stability analysis separates finite-time tracking on the ideal sliding manifold from the practical bounded response introduced by observer error and the saturation layer. Real-time implementation on a TMS320F28379D digital signal processor (DSP) demonstrates stable regulation under both steady-state and step-reference operation. At reference voltages of 40 V, 47 V, 57 V, and 87 V, the LESO–NTSMC limits output-voltage ripple to 6.7–8.9%, compared with 9.9–15.1% for conventional sliding mode control (SMC), corresponding to a 31–41% reduction. The experiments further show an average efficiency of 88.7% while requiring only output-voltage feedback, supporting a reduced-sensing solution for high-gain direct current to direct current (DC–DC) conversion in low-voltage renewable energy systems.

This is an open access article under the CC BY-SA license.

Corresponding Author:

Thanh-Lam Le
Faculty of Electrical and Electronics Engineering
Ho Chi Minh City University of Technology and Engineering
Ho Chi Minh City, Vietnam
Email: lamlethanh@hcmute.edu.vn

1. INTRODUCTION

In recent years, the global shift towards clean energy has significantly accelerated the development and deployment of renewable energy technologies, such as photovoltaic (PV) panels and fuel cells [1]–[3]. These sources offer promising solutions to reduce dependence on fossil fuels and mitigate environmental impacts. However, they typically deliver relatively low and fluctuating direct current (DC) output voltages, which pose substantial challenges for integration into power systems that require higher and more stable voltage levels [4]. This voltage mismatch necessitates the use of high-performance power electronic converters that can reliably elevate the voltage to the desired range while maintaining system efficiency and dynamic responsiveness [5], [6]. Among the available power conversion technologies, the direct current to direct current (DC–DC) boost converter remains a core interface in numerous applications including renewable energy systems, battery management, and electric vehicles (EV) [7], [8]. Nevertheless, conventional boost converters exhibit notable limitations when operated at high voltage gain conditions, such as increased switching stress, degraded efficiency due to parasitic elements, and the emergence of right-half-plane zeros that constrain transient performance [9]. These drawbacks become especially critical in high-

demand scenarios such as fast-charging EV stations or grid-tied PV inverters, where compactness, high gain, and dynamic stability are simultaneously required [10]–[12]. To address these challenges, both hardware topology innovations and advanced control strategies are necessary. While multi-stage or coupled-inductor converter topologies can enhance voltage gain, they also increase complexity and component stress [13]. Advanced model-based and sliding-mode control strategies have been investigated to improve robustness and transient performance [14]–[17]. Among them, sliding mode control (SMC) is attractive because of its robustness to matched uncertainty and straightforward implementation [15]–[17]. Non-singular terminal sliding mode controller (NTSMC) further introduces finite-time tracking dynamics while avoiding the singularity associated with conventional terminal surfaces [18]. Related robust sliding-mode designs have also been reported for electric-drive applications [19]. For example, Zheng *et al.* [18] proposed an NTSMC strategy for a conventional boost converter and demonstrated finite-time convergence with improved transient performance. However, the study was confined to the basic boost configuration and did not consider high-gain capacitor-based topologies or the lumped internal disturbances associated with such converters, thereby limiting applicability in renewable systems requiring high voltage gain. Despite these advantages, the presence of external disturbances and unmodeled internal dynamics continues to challenge the performance of SMC-based schemes, often degrading regulation accuracy in practical implementations [20], [21].

Beyond sliding-mode control, optimized closed-loop strategies for DC–DC converter systems have also been investigated [22]. Observer-based methods provide a complementary route to disturbance rejection [23]–[25]. In particular, a linear extended state observer (LESO) can estimate output-channel states and lumped unknown dynamics without requiring a detailed full-order model. The extended state observer (ESO)-based method in [24], for example, was applied to fuel-cell DC–DC converters, but it did not address the a high-gain capacitor-based boost converter (HG-CBC) topology or employ a nonlinear terminal sliding surface. In the present design, the LESO reconstructs the output-voltage derivative and lumped dynamics, whereas the NTSMC shapes the finite-time tracking dynamics on the ideal sliding manifold. This separation avoids attributing finite-time convergence to the linear observer.

This study develops an output-feedback LESO–NTSMC scheme for voltage regulation of an HG-CBC in low-voltage renewable energy systems. The main contribution is a converter-oriented integration of a signed-power non-singular surface, LESO-based recovery of the output-voltage derivative and lumped dynamics, reduced feedback sensing, and digital signal processor (DSP) implementation. The stability analysis explicitly separates ideal finite-time tracking from the practically bounded response introduced by observer error and the continuous switching approximation. Real-time hardware tests are used to evaluate steady-state regulation and dynamic operation.

2. PROBLEM FORMULATION AND MODELING

Many renewable energy sources, such as PV panels and fuel cells, deliver relatively low DC output voltages, which must be boosted to higher levels to meet system-level requirements. Traditional boost converters are often employed for this purpose, but their performance becomes severely constrained at high voltage gain settings. As the duty ratio approaches unity, these converters encounter several drawbacks including excessive switching stress, degraded efficiency due to parasitic effects, and slow transient response resulting from right-half-plane zeros. To overcome these limitations, this paper considers HG-CBC. The proposed topology employs an input inductor and a multi-stage ladder of capacitors and diodes. When the main switch is turned ON, the inductor stores energy while the ladder capacitors hold their charge. When the switch is OFF, the inductor releases its energy through intermediate stages, and capacitive charge redistribution reinforces the output voltage. This staged transfer enables substantial voltage gain without extreme duty ratios or transformer coupling. The averaged dynamic behavior of the converter is represented by a reduced set of averaged energy-storage relations. Defining the circuit variables $z_1 = i_L$, $z_2 = V_{Ca}$, and $z_3 = V_{C1}$, the representative relations used to identify the uncertain output channel are (1)-(3):

$$\frac{dz_1}{dt} = \frac{1}{L}[DV_{in} + (1-D)(V_{in} - z_2)] \tag{1}$$

$$\frac{dz_2}{dt} = \frac{1}{C_a}[(1-D)z_1 - i_{D1}] \tag{2}$$

$$\frac{dz_3}{dt} = \frac{1}{C_1}\left[i_{C2\to C1} - \frac{v_{out}}{R}\right] \tag{3}$$

where $D \in [0,1]$ is the switch duty ratio, V_{in} is the input voltage, i_{D1} is the intermediate-diode current, $i_{C2\to C1}$ is the inter-capacitor current, and R is the resistive load. The switching-dependent internal currents in (2) and (3) are not treated as independently measured states. Thus, (1)–(3) provide a reduced circuit description

rather than a closed full-order model; the omitted internal couplings, parameter variations, and parasitic effects are included in the lumped output-channel term introduced in (14).

Remark 1: the nonlinear dynamics, internal charge coupling, uncertainty in system parameters, and right-half-plane behavior make the HG-CBC a challenging system for output regulation. These characteristics necessitate the development of a robust control strategy, which will be introduced in the following section.

3. ADVANCED CONTROL STRATEGY FOR HG-CBC

A NTSMC is formulated to obtain finite-time tracking dynamics on the ideal sliding manifold. The observer-based NTSMC configuration is shown in Figure 1. To avoid the fractional-power ambiguity at negative error derivatives, the controller uses the signed-power operator in the sliding surface (4):

$$S = \xi_1 + \mu \text{sig}^{\gamma}(\xi_2) \tag{4}$$

where $\mu > 0$, $1 < \gamma < 2$, and $\text{sig}^{a}(y) = |y|^{a}\text{sgn}(y)$. The variables ξ_1 and ξ_2 denote the tracking error and its derivative, respectively:

$$\xi_1 = v_{out} - v_{ref}, \quad \xi_2 = \dot{\xi}_1 \tag{5}$$

The sliding surface $S = 0$ defines the desired system trajectory, and the control objective is to drive the system state to this manifold in finite time and keep it there.

Assumption 1: the output voltage v_{out} is measured, whereas $\dot{v}_{out}$ is supplied by the LESO introduced in section 4. The reference is piecewise constant; the analysis applies on each interval between reference updates. The input voltage is bounded and strictly positive.

To ensure the system trajectory reaches and remains on the sliding manifold, the sliding condition must hold:

$$S\dot{S} < 0 \tag{6}$$

Taking the time derivative of (4) yields:

$$\dot{S} = \dot{\xi}_1 + \mu\gamma|\xi_2|^{\gamma-1}\dot{\xi}_2 \tag{7}$$

Substituting (5) into (7) gives:

$$\dot{S} = \xi_2 + \mu\gamma|\xi_2|^{\gamma-1}\dot{\xi}_2 \tag{8}$$

Hence, the existence condition (6) becomes:

$$S\left[\xi_2 + \mu\gamma|\xi_2|^{\gamma-1}\dot{\xi}_2\right] < 0 \tag{9}$$

For the normalized output channel $\ddot{v}_{out} = b_0 u + d(t)$ introduced in (14), $\dot{\xi}_2 = b_0 u + d(t) - \ddot{v}_{ref}$. Under nominal ideal sliding, with $d(t) = 0$ and $\dot{S} = 0$, the equivalent input is (10):

$$u_{eq} = \frac{1}{b_0}\left[\ddot{v}_{ref} - \frac{1}{\mu\gamma}\text{sig}^{2-\gamma}(\xi_2)\right] \tag{10}$$

A discontinuous term is added to dominate the bounded residual uncertainty in the output-acceleration channel:

$$u = u_{eq} - \frac{k}{b_0}\text{sign}(S) \tag{11}$$

where $k > 0$ is selected above the known bound of the residual lumped disturbance. The applied duty ratio remains subject to the pulse width modulation (PWM) limits stated in section 4.

Lemma 1*:* for the signed-power surface (4), assume that the output-channel representation (14) holds, the residual disturbance is bounded, and k is sufficiently large to enforce the sliding condition. Under ideal sign switching, the trajectory reaches the sliding manifold. Once $S = 0$, the tracking error converges to zero in finite time. Proof: on $S = 0$, $\text{sig}^{\gamma}(\xi_2) = -\xi_1/\mu$, so $\xi_2 = -\mu^{-1/\gamma}\text{sig}^{1/\gamma}(\xi_1)$. For $W = \frac{1}{2}\xi_1^2$:

$$\dot{W} = -\mu^{-1/\gamma}|\xi_1|^{1+1/\gamma} < 0, \qquad \xi_1 \neq 0 \tag{12}$$

Because $0 < 1/\gamma < 1$, (12) establishes finite-time convergence of the reduced tracking dynamics on the ideal manifold. The settling time depends on the initial error; therefore, fixed-time convergence is not claimed. For continuous implementation, the sign function in (11) is replaced by the saturation function.

$$\text{sat}(S/\phi) = \begin{cases} 1 & \text{if } S > \phi \\ S/\phi & \text{if } |S| \leq \phi \\ -1 & \text{if } S < -\phi \end{cases} \tag{13}$$

where $\phi > 0$ is the boundary-layer thickness. With saturation, the trajectory is driven to the layer $|S| \leq \phi$; exact finite-time convergence to $S = 0$ is not claimed. Figure 2 compares the two switching functions.

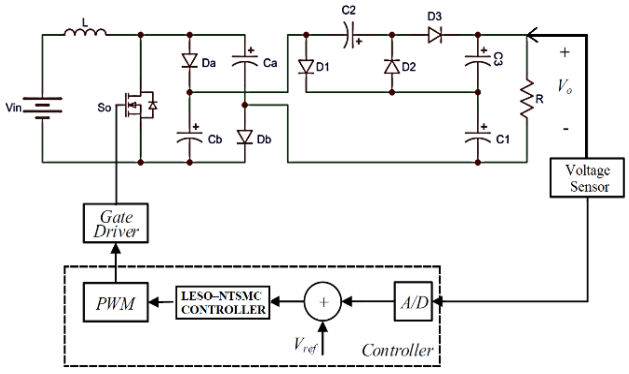


Figure 1. Configuration of the high-gain boost converter and observer-based NTSMC control loop

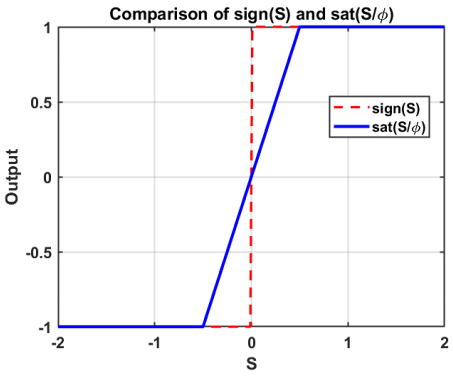


Figure 2. Comparison of sign(S) and sat(S/ϕ)

4. OBSERVER-AIDED COMPENSATION AND COMPOSITE CONTROL DESIGN

4.1. Observer-based disturbance compensation using linear extended state observer

A LESO is introduced to estimate the output-voltage derivative and the lumped output-channel dynamics from the measured output voltage. Over the considered continuous-conduction operating region, the normalized input has a known control direction and the output channel is represented as (14):

$$\ddot{v}_{out} = b_0 u + d(t), \qquad b_0 > 0 \tag{14}$$

where b_0 is the nominal input gain and $d(t)$ collects the nonlinear internal couplings, gain mismatch, parameter variation, parasitic effects, and external perturbations omitted from the reduced model.
Using $x_1 = v_{out}$ and $x_2 = \dot{v}_{out}$, (14) is written in canonical form as (15):

$$\begin{cases} \dot{x}_1 = x_2, \\ \dot{x}_2 = b_0 u + d(t). \end{cases} \tag{15}$$

here u is the normalized controller output and the applied duty ratio is $D = \text{sat}_{[0,1]}(u)$. The local stability analysis applies to the operating region in which the command does not remain saturated.
Let the extended state be defined as (16):

$$x_3 = \text{d}(t) \tag{16}$$

Then, the augmented system becomes (17):

$$\begin{cases} \dot{x}_1 = x_2 \\ \dot{x}_2 = b_0 u + x_3 \\ \dot{x}_3 = \dot{d}(t) \end{cases} \tag{17}$$

The LESO is constructed as (18):

$$\begin{cases} \dot{\hat{x}}_1 = \hat{x}_2 + \beta_1(x_1 - \hat{x}_1) \\ \dot{\hat{x}}_2 = b_0 u + \hat{x}_3 + \beta_2(x_1 - \hat{x}_1) \\ \dot{\hat{x}}_3 = \beta_3(x_1 - \hat{x}_1) \end{cases} \tag{18}$$

where $\hat{x}_1, \hat{x}_2, \hat{x}_3$ are the estimated output voltage, its derivative, and total disturbance, respectively. The gains $\beta_1, \beta_2, \beta_3$ are chosen such that the characteristic polynomial:

$$s^3 + \beta_1 s^2 + \beta_2 s + \beta_3 \tag{19}$$

is Hurwitz (i.e., all roots have negative real parts), ensuring observer stability.
Definition 1: the observer bandwidth $\omega_o > 0$ is introduced to define the observer gains as (20):

$$\beta_1 = 3\omega_o, \qquad \beta_2 = 3\omega_o^2, \qquad \beta_3 = \omega_o^3 \tag{20}$$

which places the observer poles at $s = -\omega_o$.

The estimated disturbance is fed forward to compensate for the lumped dynamics. For output-feedback implementation, u_{eq} in (10) is evaluated with the LESO state estimates, and the composite law is:

$$u = u_{eq} - \frac{1}{b_0}\left[k\text{sat}\left(\frac{\hat{S}}{\phi}\right) + \hat{x}_3\right] \tag{21}$$

where $\hat{S}$ is defined in (26). The term $\hat{x}_3/b_0$ compensates the estimated lumped dynamics, while the saturation term limits switching activity.

Remark 2: increasing ω_o accelerates estimation but amplifies measurement noise. A practical sequence is to select ω_o from the sampling and noise bandwidth, tune μ and γ for the desired tracking profile, choose k above the residual uncertainty bound, and then select ϕ to balance ripple and accuracy. With a time-varying disturbance, LESO errors are bounded rather than exactly zero.

4.2. Stability of the composite observer-based non-singular terminal sliding mode controller system

This subsection establishes practical stability of the composite LESO–NTSMC system. Finite-time tracking refers to the reduced dynamics on the ideal sliding manifold; with a time-varying disturbance and a saturation layer, the closed-loop tracking and estimation errors are shown to remain ultimately bounded. The output-channel dynamics are (22):

$$\dot{x}_1 = x_2, \qquad \dot{x}_2 = b_0 u + d(t) \tag{22}$$

where $x_1 = v_{out}$, $x_2 = \dot{v}_{out}$, u is defined in (21), $b_0 > 0$ is the nominal input gain, and $d(t)$ is the lumped term defined in (14).

The LESO reconstructs the system states and the disturbance in real time, yielding the estimates $\hat{x}_1, \hat{x}_2, \hat{x}_3$, where $\hat{x}_3 \approx d(t)$. Define the estimation errors as (23):

$$e_1 = x_1 - \hat{x}_1, \quad e_2 = x_2 - \hat{x}_2, \quad e_3 = d(t) - \hat{x}_3 \tag{23}$$

From the LESO dynamics (18), the estimation-error dynamics are (24):

$$\begin{cases} \dot{e}_1 = e_2 - \beta_1 e_1 \\ \dot{e}_2 = e_3 - \beta_2 e_1 \\ \dot{e}_3 = \dot{d}(t) - \beta_3 e_1 \end{cases} \tag{24}$$

Assume that $|\dot{d}(t)| \le L_d$, with $L_d > 0$. Since the homogeneous error matrix associated with (24) is Hurwitz, the zero-input observer error decays exponentially. For nonzero bounded $\dot{d}(t)$, the estimation errors are uniformly ultimately bounded and converge exactly to zero only when $\dot{d}(t) = 0$.
The sliding surface is defined as (25):

$$S = \xi_1 + \mu\text{sig}^{\gamma}(\xi_2) = \left(x_1 - v_{ref}\right) + \mu\text{sig}^{\gamma}\left(x_2 - \dot{v}_{ref}\right) \tag{25}$$

The estimated sliding surface is (26):

$$\hat{S} = \left(\hat{x}_1 - v_{ref}\right) + \mu\text{sig}^{\gamma}\left(\hat{x}_2 - \dot{v}_{ref}\right) \tag{26}$$

Define the sliding surface estimation error as (27):

$$\varepsilon_S = S - \hat{S} \tag{27}$$

Applying first-order Taylor approximation around $\hat{x}_2$, we obtain:

$$\varepsilon_S \approx e_1 + \mu\gamma\left|\hat{x}_2 - \dot{v}_{ref}\right|^{\gamma-1} e_2 \tag{28}$$

The composite control input from (21) is (29):

$$u = u_{eq} - \frac{1}{b_0}\left[k\text{sat}\left(\frac{\hat{S}}{\phi}\right) + \hat{x}_3\right] \tag{29}$$

Let $e = [e_1, e_2, e_3]^T$ and let A_o denote the Hurwitz error matrix in (24). For any $Q = Q^T > 0$, there exists $P = P^T > 0$ satisfying $A_o^T P + P A_o = -Q$. Using (29) with $V_c = \frac{1}{2}S^2 + e^T P e$, Young's inequality yields, for gains that dominate the observer-induced coupling, $\dot{V}_c \leq -c_1 \Psi_\phi(S) - c_2 \parallel e \parallel^2 + c_3 L_d^2 + c_4 \phi^2$, where $c_i > 0$ and $\Psi_\phi(S) = \min\{|S|, S^2/\phi\}$. Thus, S and e are uniformly ultimately bounded, and the tracking states remain bounded. In the ideal limiting case $\dot{d}(t) = 0$ and $\phi \to 0$, the observer error converges exponentially and the reduced tracking error converges in finite time. Fixed-time convergence and finite-time convergence of the LESO error are not claimed.

5. EXPERIMENTAL VALIDATION

To validate the controller experimentally, the hardware platform shown in Figure 3 was assembled around a Texas Instruments TMS320F28379D DSP for real-time control. The controller was developed in MATLAB/Simulink and deployed to the DSP using automatic code generation. The prototype follows the HG-CBC configuration in Figure 1, with components selected according to their voltage, current, and thermal ratings. The energy-storage network comprises capacitors $C_a, C_b, C_2, C_o = 220\,\mu F$ and $C_1 = 470\,\mu F$. The converter uses a single input inductor of $L = 420\,\mu H$. The N-channel metal-oxide-semiconductor field-effect transistor (MOSFET) is rated at 150 V and 104 A and was selected for low $R_{DS(on)}$ and fast switching. The freewheeling and boost diodes are rated at 600 V and 30 A, respectively. Experiments were conducted with a resistive load of $R = 100\,\Omega$, and the input voltage V_{in} was fixed at $12\,V_{DC}$ throughout the tests. The DSP analog-to-digital converter (ADC) channels acquired the signals required for monitoring and performance evaluation; only the output-voltage measurement was used by the proposed feedback controller. Real-time waveforms were recorded with the oscilloscope and host PC shown in Figure 3. The hardware test bench therefore includes practical effects such as electromagnetic interference, sensor noise, propagation delay, and parasitic elements. The conventional SMC was implemented as the baseline for comparison, and both controllers were evaluated at the same steady-state output-voltage references.

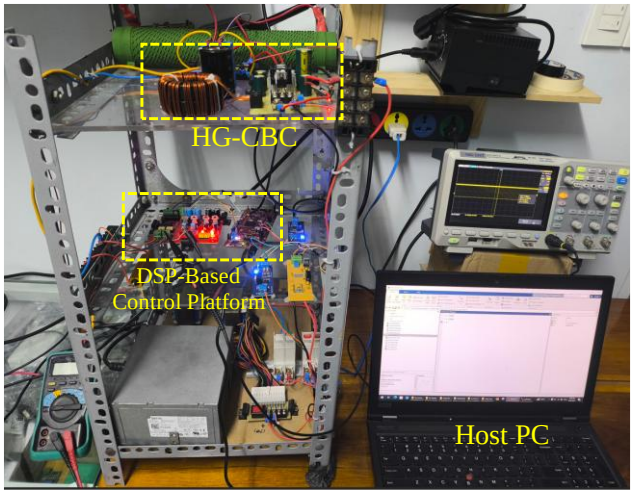


Figure 3. Experimental test setup

Figures 4(a) to (d) show the steady-state responses of the proposed LESO–NTSMC controller at 40 V, 47 V, 57 V, and 87 V, respectively. Figures 5(a) to (d) show the corresponding responses of the conventional SMC at the same reference voltages, with consistently larger output-voltage ripple. Figure 6 quantifies this difference: the LESO–NTSMC ripple is approximately 8.9%, 8.0%, 6.7%, and 6.8% at 40 V, 47 V, 57 V, and 87 V, respectively, compared with 15.1%, 13.4%, 11.3%, and 9.9% for conventional SMC. These values correspond to a ripple reduction of approximately 31–41% over the tested range. Table 1 summarizes the steady-state comparison and the feedback measurements required by each controller.

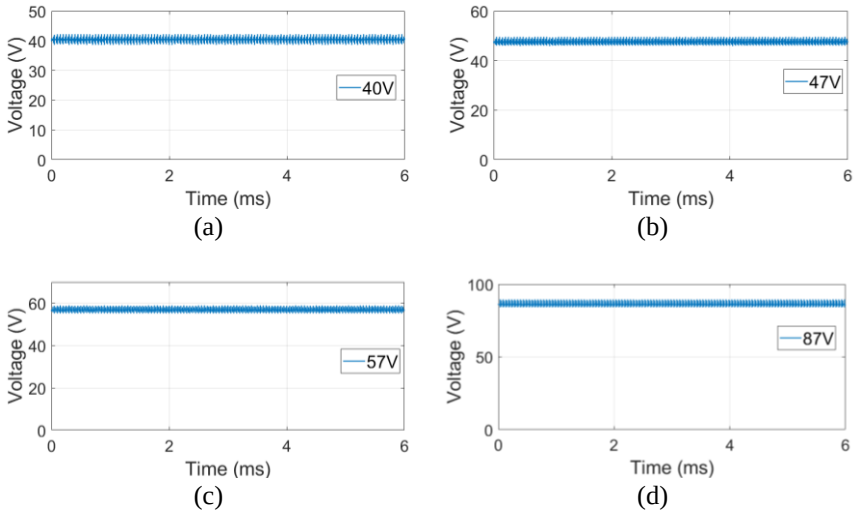


Figure 4. Steady-state output voltage waveforms of the proposed LESO–NTSMC controller at different reference voltages: (a) 40 V, (b) 47 V, (c) 57 V, and (d) 87 V

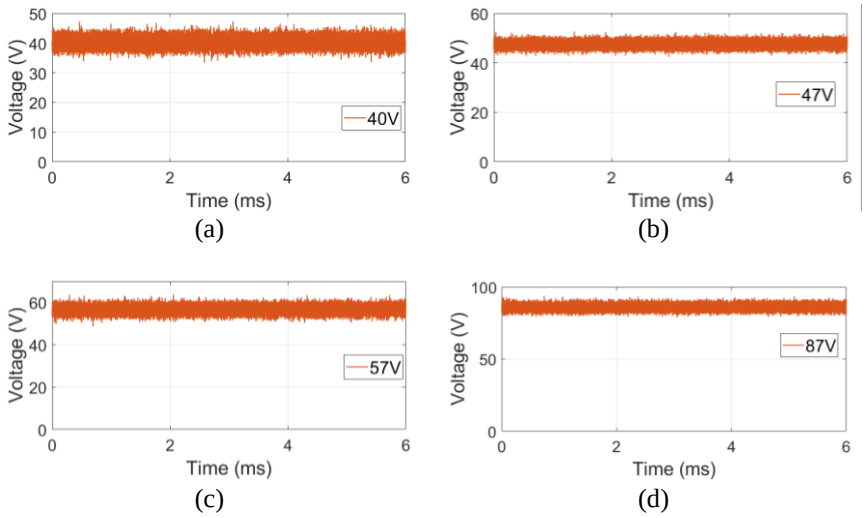


Figure 5. Steady-state output voltage waveforms of the conventional SMC controller at different reference voltages: (a) 40 V, (b) 47 V, (c) 57 V, and (d) 87 V

Together with the steady-state results in Figures 4–6, the dynamic response, current behavior, and efficiency of the HG-CBC with the proposed controller were evaluated over the tested operating range, as presented in Figure 7. Figure 7(a) shows the input and output voltages under step changes in the voltage reference. The input voltage remains close to 12 V, while the output voltage follows the commanded levels. Figure 7(b) shows the corresponding input and output currents, which remain bounded under the applied load. Figure 7(c) presents the measured efficiency, which averages approximately 88.7% over the test interval.

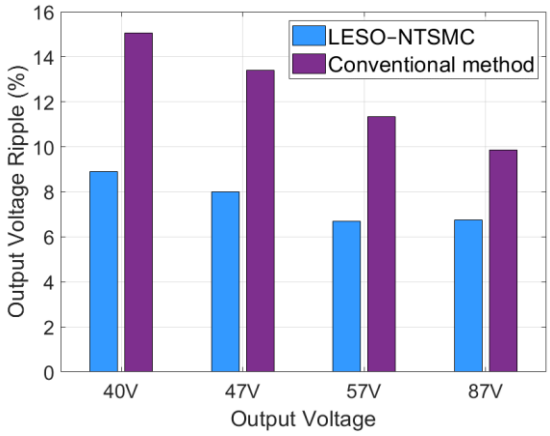


Figure 6. Output-voltage ripple comparison between LESO–NTSMC and conventional SMC at reference voltages of; 40 V, 47 V, 57 V, and 87 V

Table 1. Experimental comparison between LESO–NTSMC and conventional SMC

Metric	LESO–NTSMC	Conventional SMC
Voltage ripple (%)	6.7–8.9	9.9–15.1
Steady-state regulation	Stable and lower ripple	Stable and higher ripple
Feedback measurements	Output voltage only	Output voltage and inductor current

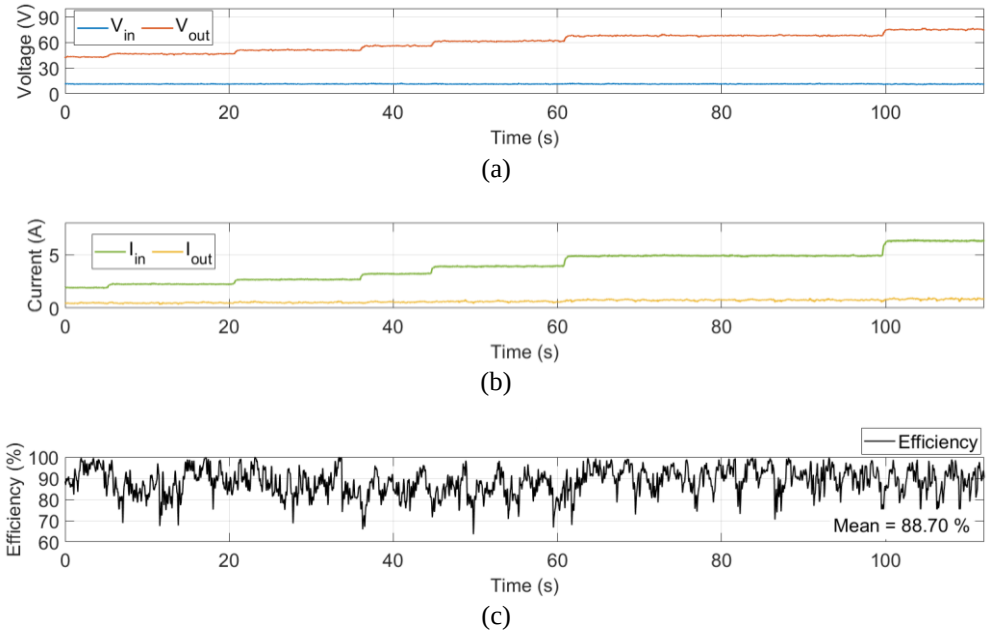


Figure 7. Dynamic response of the proposed LESO–NTSMC controller: (a) input and output voltages under step reference changes, (b) input and output currents, and (c) measured efficiency

6. CONCLUSION

The LESO–NTSMC scheme provides output-feedback voltage regulation for the HG-CBC using a signed-power non-singular sliding surface and an LESO that reconstructs the output-voltage derivative and lumped dynamics from the measured voltage. The analysis establishes finite-time reduced tracking dynamics on the ideal sliding manifold and practical boundedness when observer error and the saturation layer are included. DSP experiments confirm stable regulation over the tested reference range, with output-voltage ripple reduced by approximately 31–41% relative to conventional SMC. The resulting controller therefore offers a reduced-sensing implementation for high-gain DC–DC conversion within the stated operating region.

FUNDING INFORMATION

The authors received no specific funding for this work.

AUTHOR CONTRIBUTIONS STATEMENT

This journal uses the Contributor Roles Taxonomy (CRediT) to recognize individual author contributions, reduce authorship disputes, and facilitate collaboration.

Name of Author	C	M	So	Va	Fo	I	R	D	O	E	Vi	Su	P	Fu
Thanh-Lam Le	✓	✓	✓	✓	✓	✓	✓	✓	✓	✓	✓	✓	✓	✓
Nguyen Thi Bich Mai			✓			✓		✓		✓	✓			✓

C : **C**onceptualization
M : **M**ethodology
So : **So**ftware
Va : **Va**lidation
Fo : **Fo**rmal analysis
I : **I**nvestigation
R : **R**esources
D : **D**ata Curation
O : Writing - **O**riginal Draft
E : Writing - Review & **E**diting
Vi : **Vi**sualization
Su : **Su**pervision
P : **P**roject administration
Fu : **Fu**nding acquisition

CONFLICT OF INTEREST STATEMENT

Authors state no conflict of interest.

DATA AVAILABILITY

The data supporting the findings of this study are available from the corresponding author upon reasonable request.

REFERENCES

[1] A. M. Mitrašinović, "Photovoltaics advancements for transition from renewable to clean energy," *Energy*, vol. 237, p. 121510, Dec. 2021, doi: 10.1016/j.energy.2021.121510.
[2] M. Victoria *et al*., "Solar photovoltaics is ready to power a sustainable future," *Joule*, vol. 5, no. 5, pp. 1041–1056, May 2021, doi: 10.1016/j.joule.2021.03.005.
[3] T.-Z. Ang, M. Salem, M. Kamarol, H. S. Das, M. A. Nazari, and N. Prabaharan, "A comprehensive study of renewable energy sources: Classifications, challenges and suggestions," *Energy Strategy Reviews*, vol. 43, p. 100939, Sep. 2022, doi: 10.1016/j.esr.2022.100939.
[4] L. Meegahapola, A. Sguarezi, J. S. Bryant, M. Gu, E. R. C. D., and R. B. A. Cunha, "Power system stability with power-electronic converter interfaced renewable power generation: Present issues and future trends," *Energies*, vol. 13, no. 13, p. 3441, Jul. 2020, doi: 10.3390/en13133441.
[5] T. L. Le, "Firefly Algorithm-based Optimization of Control Parameters in DC Conversion Systems," *Engineering, Technology and Applied Science Research*, vol. 15, no. 2, pp. 20588–20594, Apr. 2025, doi: 10.48084/etasr.9606.
[6] P. Arévalo, D. Ochoa-Correa, and E. Villa-Ávila, "Towards Energy Efficiency: Innovations in High-Frequency Converters for Renewable Energy Systems and Electric Vehicles," *Vehicles*, vol. 7, no. 1, p. 1, 2025, doi: 10.3390/vehicles7010001.
[7] S. Habib *et al*., "Contemporary trends in power electronics converters for charging solutions of electric vehicles," *CSEE Journal of Power and Energy Systems*, vol. 6, no. 4, pp. 911–929, 2020, doi: 10.17775/CSEEJPES.2019.02700.
[8] J. Wang, B. Wang, L. Zhang, J. Wang, N. I. Shchurov, and B. V. Malozyomov, "Review of bidirectional DC–DC converter topologies for hybrid energy storage system of new energy vehicles," *Green Energy and Intelligent Transportation*, vol. 1, no. 2, p. 100010, Sep. 2022, doi: 10.1016/j.geits.2022.100010.
[9] M. Forouzesh, Y. P. Siwakoti, S. A. Gorji, F. Blaabjerg, and B. Lehman, "Step-Up DC–DC Converters: A Comprehensive Review of Voltage-Boosting Techniques, Topologies, and Applications," *IEEE Transactions on Power Electronics*, vol. 32, no. 12, pp. 9143–9178, Dec. 2017, doi: 10.1109/TPEL.2017.2652318.
[10] D. Nayanasiri and Y. Li, "Step-Down DC–DC Converters: An Overview and Outlook," *Electronics (Switzerland)*, vol. 11, no. 11, p. 1693, May 2022, doi: 10.3390/electronics11111693.
[11] F. J. Blázquez-Plaza, A. Barrado, and M. Wijnen, "Survey of high-voltage DC/DC converters for electrospray thrusters," *CEAS Space Journal*, vol. 18, no. 1, pp. 1–18, Jan. 2026, doi: 10.1007/s12567-025-00615-w.
[12] J. Saha, N. Kumar, and S. K. Panda, "Adaptive Grid-Supportive Control for Solar-Power Integrated Electric-Vehicle Fast Charging Station," *IEEE Transactions on Energy Conversion*, vol. 38, no. 3, pp. 2034–2044, Sep. 2023, doi: 10.1109/TEC.2023.3260191.
[13] H. Khalid *et al*., "A High Voltage Gain Multi-Stage DC-DC Boost Converter with Reduced Voltage Stress," *IETE Journal of Research*, vol. 70, no. 2, pp. 2032–2046, Feb. 2024, doi: 10.1080/03772063.2022.2143440.
[14] Y. Li, S. Sahoo, T. Dragičević, Y. Zhang, and F. Blaabjerg, "Stability-Oriented Design of Model Predictive Control for DC/DC Boost Converter," *IEEE Transactions on Industrial Electronics*, vol. 71, no. 1, pp. 922–932, Jan. 2024, doi: 10.1109/TIE.2023.3247785.
[15] A. F. Murtaza, H. A. Sher, F. U. Khan, A. Nasir, and F. Spertino, "Efficient MPP Tracking of Photovoltaic (PV) Array Through Modified Boost Converter With Simple SMC Voltage Regulator," *IEEE Transactions on Sustainable Energy*, vol. 13, no. 3, pp. 1790–1801, Jul. 2022, doi: 10.1109/TSTE.2022.3172315.

[16] A. Goudarzian and A. Khosravi, "A unified method to the design of an improved high frequency sliding mode current controller for DC/DC boost converter in continuous current condition based on analogue implementation," *Sadhana - Academy Proceedings in Engineering Sciences*, vol. 45, no. 1, p. 281, Dec. 2020, doi: 10.1007/s12046-020-01507-x.
[17] G. E. Mejia-Ruiz, M. R. A. Paternina, J. A. de la O Serna, and A. Zamora-Mendez, "O Splines-Based Fixed-Frequency Integral Sliding-Mode Controller for PFC Rectifier," *IEEE Transactions on Power Electronics*, vol. 38, no. 8, pp. 9448–9458, Aug. 2023, doi: 10.1109/TPEL.2023.3270268.
[18] S. Zheng, M. Qi, Y. Shu, Y. Wang, and J. Lang, "Non-singular terminal sliding mode control strategy for DC/DC Boost converter system using a finite-time convergent observer," *IET Power Electronics*, vol. 15, no. 16, pp. 1868–1876, Dec. 2022, doi: 10.1049/pel2.12354.
[19] Z. Zhang, X. Yang, W. Wang, K. Chen, N. C. Cheung, and J. Pan, "Enhanced Sliding Mode Control for PMSM Speed Drive Systems Using a Novel Adaptive Sliding Mode Reaching Law Based on Exponential Function," *IEEE Transactions on Industrial Electronics*, vol. 71, no. 10, pp. 11978–11988, Oct. 2024, doi: 10.1109/TIE.2023.3347845.
[20] Q. Ullah, T. D. C. Busarello, D. I. Brandao, and M. G. Simões, "Design and Performance Evaluation of SMC-Based DC–DC Converters for Microgrid Applications," *Energies*, vol. 16, no. 10, p. 4212, May 2023, doi: 10.3390/en16104212.
[21] H. Zhang *et al.*, "Fast Terminal Sliding Mode Control of DC–DC Boost Converters With Enhanced Disturbance Rejection," *IEEE Journal of Emerging and Selected Topics in Power Electronics*, vol. 12, no. 1, pp. 531–542, Feb. 2024, doi: 10.1109/JESTPE.2023.3336741.
[22] S. Y. Chen, B. C. Yang, T. A. Pu, C. H. Chang, and R. C. Lin, "Active Current Sharing of a Parallel DC-DC Converters System Using Bat Algorithm Optimized Two-DOF PID Control," *IEEE Access*, vol. 7, pp. 84757–84769, 2019, doi: 10.1109/ACCESS.2019.2925064.
[23] B. Guo, S. Bacha, M. Alamir, A. Hably, and C. Boudinet, "Generalized Integrator-Extended State Observer with Applications to Grid-Connected Converters in the Presence of Disturbances," *IEEE Transactions on Control Systems Technology*, vol. 29, no. 2, pp. 744–755, Mar. 2021, doi: 10.1109/TCST.2020.2981571.
[24] S. Zhuo, A. Gaillard, L. Xu, D. Paire, and F. Gao, "Extended State Observer-Based Control of DC-DC Converters for Fuel Cell Application," *IEEE Transactions on Power Electronics*, vol. 35, no. 9, pp. 9923–9932, Sep. 2020, doi: 10.1109/TPEL.2020.2974556.
[25] H. Zhang, J. Xian, J. Shi, S. Wu, and Z. Ma, "High Performance Decoupling Current Control by Linear Extended State Observer for Three-Phase Grid-Connected Inverter with an LCL Filter," *IEEE Access*, vol. 8, pp. 13119–13127, 2020, doi: 10.1109/ACCESS.2020.2965650.

BIOGRAPHIES OF AUTHORS



Thanh-Lam Le received the M.S. degree in Electrical Engineering from Ho Chi Minh City University of Technology, Vietnam, and the Ph.D. degree in Electrical Engineering from National Cheng Kung University, Tainan, Taiwan. He is currently a lecturer with the Faculty of Electrical and Electronics Engineering, Ho Chi Minh City University of Technology and Engineering, Vietnam. His research interests include motor drives, energy conversion systems, advanced control theory, and its applications. He can be contacted at email: lamlethanh@hcmute.edu.vn.



Nguyen Thi Bich Mai received the B.S. degree and the M.S. degree in Electrical Engineering from Ho Chi Minh City University of Technology and Education, Vietnam. She is currently a lecturer with the Faculty of Electrical and Electronics Engineering, Ho Chi Minh City University of Technology and Engineering, Vietnam. Her research interests include electrical machine simulation and control, data analysis in electrical apparatus, and intelligent control. She can be contacted at email: maintb@hcmute.edu.vn.